

# Laser-Induced Graphene for Flexible and Embeddable Gas Sensors

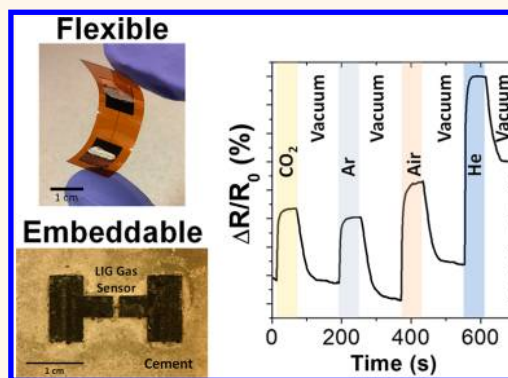
Michael G. Stanford,<sup>†</sup> Kaichun Yang,<sup>||</sup> Yieu Chyan,<sup>†</sup> Carter Kittrell,<sup>†</sup> and James M. Tour<sup>\*,†,‡,§</sup>

<sup>†</sup>Department of Chemistry, <sup>‡</sup>Smalley-Curl Institute and the NanoCarbon Center, <sup>§</sup>Department of Materials Science and NanoEngineering, and <sup>||</sup>Civil Engineering Department, Rice University, 6100 Main Street, Houston, Texas 77005, United States

## Supporting Information

**ABSTRACT:** Laser-induced graphene (LIG) has received much attention since it enables simple and rapid synthesis of porous graphene. This work presents a robust direct-write LIG-based gas sensor, which senses gases based on thermal conductivity, similar to a katharometer sensor. The gas sensors are fabricated by lasing polyimide substrates with a 10.6  $\mu\text{m}$  CO<sub>2</sub> laser to synthesize LIG. This enables the formation of flexible gas sensors which could be incorporated on a variety of surfaces. High surface area and thermal conductivity of the LIG results in rapid response times for all studied gases. The gas sensors are also embedded in cement to form a refractory composite material. These sensors are used to determine composition of various gas mixtures, such as N<sub>2</sub> and CO<sub>2</sub>, which are the most abundant gaseous species in flue gas. Thus, LIG based embeddable sensors could be incorporated in composites to enable electronically functional construction materials.

**KEYWORDS:** laser-induced graphene, flexible gas sensors, embeddable gas sensors, rapid response, LIG



Graphene is a two-dimensional (2D) material which is composed of sp<sup>2</sup>-hybridized carbon.<sup>1,2</sup> Impressive materials properties have been demonstrated, such as extremely high charge mobility,<sup>3</sup> mechanical strength,<sup>4,5</sup> and thermal conductivity.<sup>6</sup> However, difficulty in large-area synthesis and the requisite transfer of the graphene to device surfaces has slowed the incorporation of graphene into device embodiments. Recently, 3D porous graphene has been synthesized in a direct-write manner simply by lasing various carbon sources with an infrared laser that is part of commercial systems found in most machine shops.<sup>7</sup> This material is referred to as laser-induced graphene (LIG). By controlling atmospheric conditions during synthesis, LIG can be tuned from superhydrophilic to superhydrophobic.<sup>8</sup> Microstructures ranging from networks of graphene sheets to networks of graphene fibers and even nanodiamond formation can also be achieved by controlling lasing conditions.<sup>9,10</sup> LIG has been used in applications such as supercapacitors,<sup>11–13</sup> strain and wearable body-condition sensors,<sup>14,15</sup> and electrocatalysis<sup>16–18</sup> to name a few, and we have recently reviewed the topic.<sup>19,20</sup>

Two-dimensional graphene has demonstrated potential as a gas sensing material.<sup>21</sup> Owing to the high surface area to volume ratio and its ballistic transport, the electronic properties of graphene can be significantly altered by gas chemisorption or even physisorption. This has enabled graphene to detect gases with a high degree of precision, and these gases include NH<sub>3</sub>,<sup>22,23</sup> SO<sub>2</sub>,<sup>24</sup> H<sub>2</sub>,<sup>25</sup> and NO<sub>2</sub>.<sup>26</sup> Conveniently, LIG possesses high surface area ( $\sim 350 \text{ m}^2$

$\text{g}^{-1}$ )<sup>7</sup> due its 3D porous structure, which supplies many surface sites for gas–solid interactions, and it is conveniently prepared on flexible commercial polyimide (PI) films. Therefore, LIG is a promising candidate for many gas sensing applications. Applicable to this work, thermal conductivity detectors (TCDs) are gas sensors that detect changes in thermal conductivity and hence composition of a gas species. TCDs use a hot filament that is exposed to gas. Composition-induced fluctuations in thermal conductivity of the surrounding medium influences the temperature and consequently the resistivity of the hot filament. Monitoring the filament resistance provides means to detect the presence of an analyte. To date, TCDs have been used in applications such as a gas sensor in gas chromatography systems<sup>27</sup> as well as monitoring coolant gases for gas-cooled turbo generators.

In this work, LIG was synthesized on a PI substrate to rapidly fabricate flexible arrays of gas sensors that detect a broad range of gases based on their thermal conductivity, similar to a TCD or katharometer.<sup>28</sup> The resistive gas sensors exhibit fast response times of 7–8 s, limited here by the gas introduction time into the test chamber, for all tested gases. The fast response time is attributed to the large surface area of the LIG as well as high thermal conductivity in comparison to common filament materials. LIG/cement composites were also

**Received:** December 20, 2018

**Accepted:** March 4, 2019

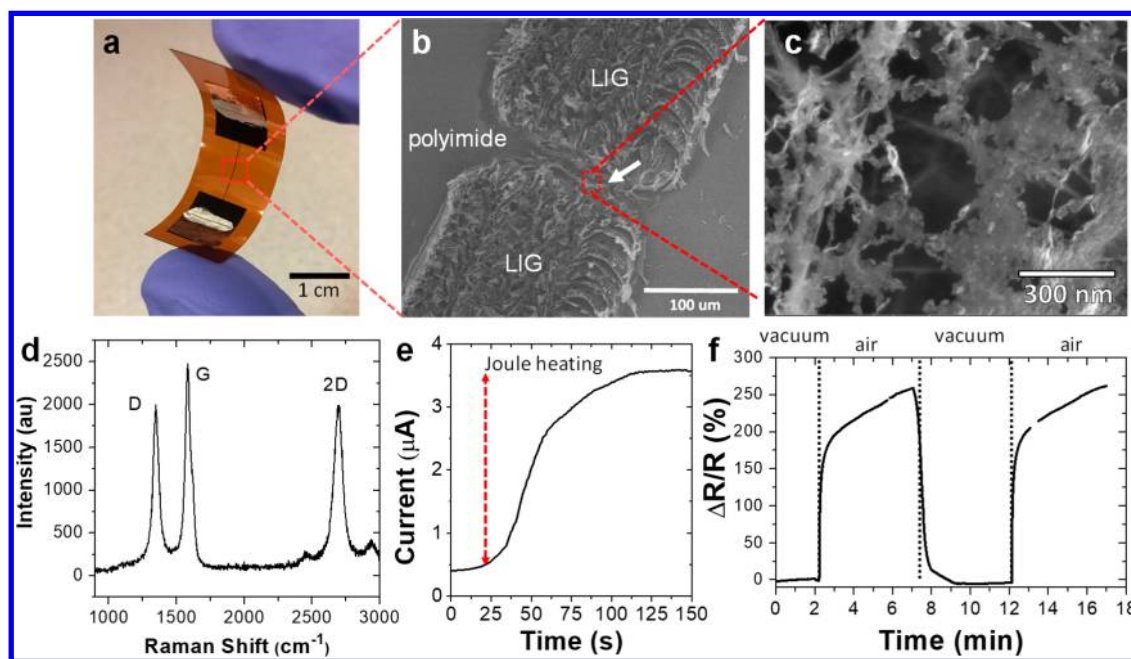


**Figure 1.** (a) Optical image of LIG-based Type 1 gas sensor on PI substrate. (b,c) SEM image of  $\sim 20 \mu\text{m}$  channel in LIG device. LIG filaments, denoted by the white arrow, span between the LIG electrodes. (d) Raman spectra of LIG confirm graphene formation. (e) Device current after applying a voltage source (5 V) that then results in Joule heating. (f) Response (change is resistance) of the gas sensor when exposed to air. Sensor voltage ( $V_s$ ) = 5 V.

formed, which enables sensors to be embedded within construction or refractory materials. The flexible and embeddable gas sensors demonstrate the capability to determine gas compositions and represent a step toward realizing “smart” composite construction materials.

## RESULTS AND DISCUSSION

Figure 1a shows an example of a flexible gas sensor (Type 1) that has been synthesized by irradiating a PI substrate with the  $10.6 \mu\text{m}$  laser to generate LIG. This device consists of LIG electrodes ( $\sim 200 \mu\text{m}$  in width) that span between two larger pads, which are used as contacts that are also composed of LIG (Figure 1b). A gap of  $\sim 20 \mu\text{m}$  was intentionally left between the electrodes, however, small filaments of LIG (denoted by the inset white arrow) overlap the gap and provide a path for electrical transport. A high-resolution SEM image of the region where nanoscale filaments overlap is reported in Figure 1c. The LIG is also highly porous, which results in an extremely high surface area. A Raman spectrum shown in Figure 1d shows a sharp single 2D peak centered  $\sim 2697 \text{ cm}^{-1}$ , which confirms that the LIG is indeed composed of graphene. The peak is distinct from that of graphite which is composed of the  $2\text{D}_1$  and  $2\text{D}_2$  peaks which are typically upshifted in comparison to graphene ( $\sim 2725 \text{ cm}^{-1}$ ).<sup>29</sup>

The operating mechanism for gas sensors relies on Joule heating of the LIG particles spanning the device gap, which subsequently transfers heat to its surroundings via convective heat loss by Newton’s law of cooling in eq 1:

$$q = hA(T_a - T_b) \quad (1)$$

where  $q$  is the heat transferred,  $h$  is the heat transfer coefficient,  $A$  is the surface area of the LIG, and  $T_a$  and  $T_b$  are the temperature of gas molecules and LIG filament, respectively.<sup>30</sup> The heat transfer coefficient,  $h$ , is dependent upon the material parameters, such as thermal conductivity ( $\kappa$ ), viscosity ( $\mu$ ), and

heat capacity ( $c_p$ ). When a voltage is applied across the LIG device, Joule heating, which is proportional to the power ( $P$ ) dissipated in the material ( $P \propto I^2R$ , where  $I$  is current and  $R$  is resistance), is localized around the filament region due to its large resistance. Therefore, the Joule heating of the gas sensor is almost completely localized at the microgap between the two LIG electrodes, where small particles of LIG span the two electrodes. Thermogravimetric analysis (TGA) of LIG reveals that it decomposes in air at a temperature of  $\sim 850 \text{ K}$  (Figure S1), hence the gas sensor should be operated below this temperature. To confirm the presence of Joule heating under applied voltage, the current of the gas sensor was monitored as a function of time and reported in Figure 1e in vacuum. Immediately after the potential was applied, the device resistance decreased by approximately 800%. The temperature-dependent transport properties of the LIG (Figure S2a) show that the resistivity of the LIG decreases with increasing temperature over the relevant temperatures. This correlation confirms that the LIG filament is increasing in temperature due to Joule heating. When exposed to air, the temperature of the LIG filament is reduced due to convective heat transfer. This results in increased resistance in the sensor when exposed to gas molecules. It is worth noting that the PI is a high temperature polymer which is stable up to  $\sim 820 \text{ K}$ ; thus, the PI substrate does not experience significant degradation during sensor operation. Figure 1f shows the device sensitivity (change in resistance) when exposed to air after being held in vacuum. Resistivity of the sensor increases by  $>250\%$  when exposed to air due to convective cooling of the LIG filament. Multiple cycles of exposure to air and vacuum are shown in Figure 1f.

In order to controllably tune the resistivity of Type 1 gas sensors and increase the sensitivity, the device was exposed to oxygen plasma to etch away the LIG and finely tune the size of the LIG filaments (Figure S4). This enables tuning of the

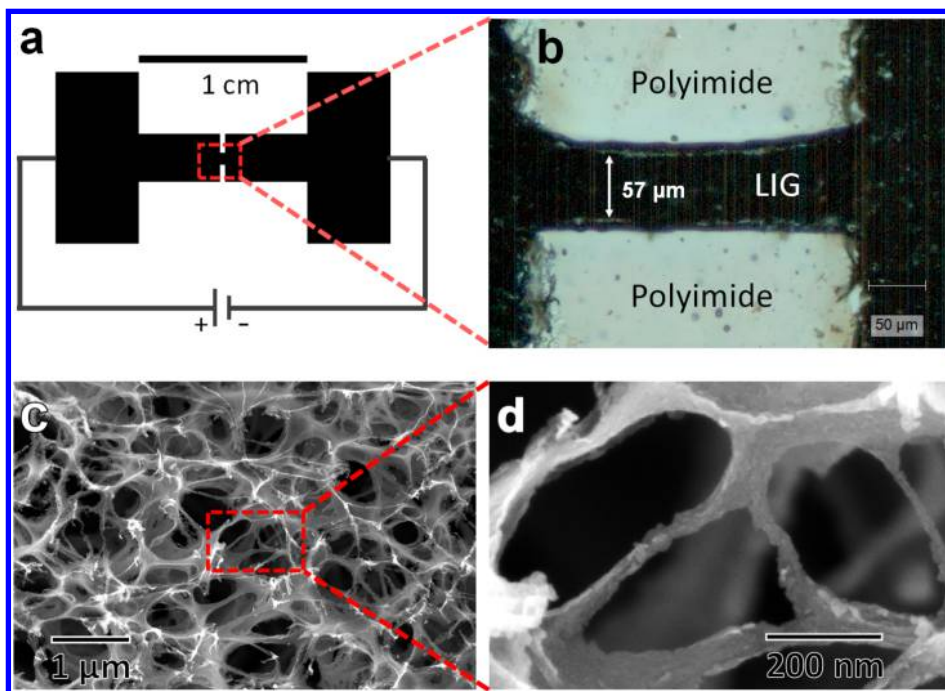


Figure 2. (a) Schematic of the Type 2 gas sensor with a LIG filament. All black portions represent LIG. The active region is out of scale to increase visibility in this schematic. (b) Optical image of the LIG filament that is 57  $\mu\text{m}$  in width. (c,d) SEM images of the porous LIG which is composed of nanofilaments.

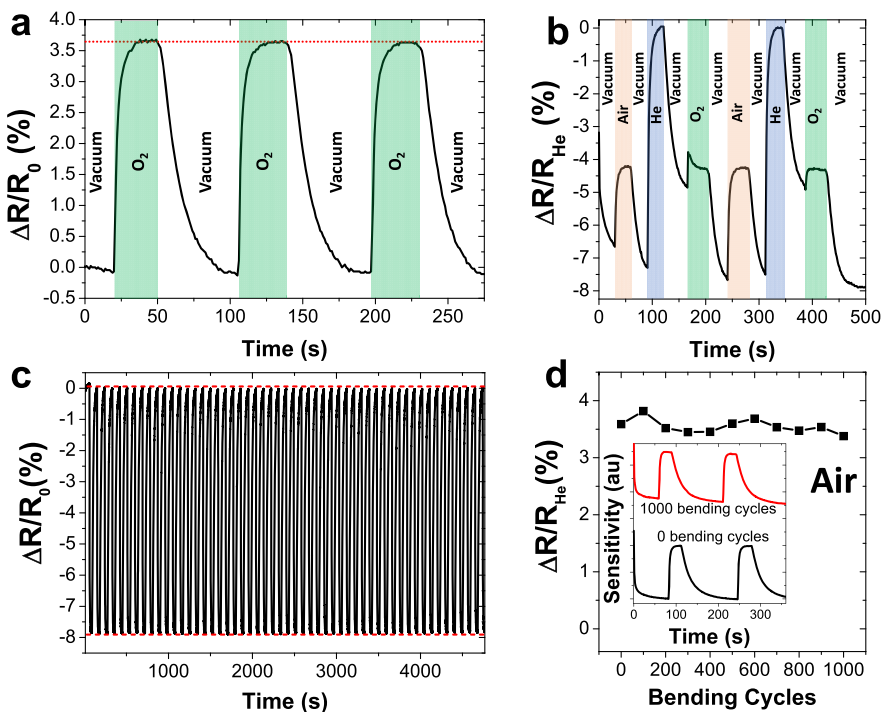


Figure 3. (a, b) Responses of the Type 2 sensor at 12 V to a variety of gases, showing repeatability. Shaded regions indicate when the sensor was exposed to the various gases. (c) Response of the gas sensor to >50 cycles of He and vacuum. (d) Magnitude of response of gas sensor to air after bending it with a radius of curvature of 7 mm. Inset figure shows the response of the gas sensor to air after 0 and 1000 bending cycles.

device resistance by increasing the extent of Joule heating in the LIG filaments. Device properties as a function of the plasma exposure time and SEM images can be found in Figure S4. Due to the low operating current of this device, power consumption is only  $\sim 20 \mu\text{W}$ . However, there was a significant degree of variation in the sensitivity of the Type 1 devices

fabricated under identical conditions ( $\pm 90\%$  sensor sensitivity), and only  $\sim 20\%$  of devices were functional. This is because Type 1 sensors rely on the pseudorandom formation of nanoscale LIG filaments to span the channel between LIG electrodes. Subtle changes in the amount and orientation of the LIG filaments which span the gap between electrodes can

result in significant variation in Joule heating and hence device sensitivity. It is worth noting that mechanical activation of nonfunctioning devices could be achieved by scratching across the polyimide channel with a scalpel (Figure S5); however, this process is likely unreliable.

Since the Type 1 sensors exhibit a large degree of variation in device sensitivity, a more robust design (Figure 2a) was subsequently adapted for LIG gas sensors that made the extent of Joule heating more controllable (Type 2 sensor), although sacrificing some of the device sensitivity. Namely, device sensitivities compared to vacuum of greater than 250% in air were achieved with Type 1 sensors, compared to an average sensitivity of  $\sim 3.9\%$  for Type 2 sensors. However, device repeatability was improved from Type 1 to Type 2 sensors from  $\sim 20\%$  to 100%, respectively. Additional statistics on device repeatability can be found in the Supporting Information.

The Type 2 sensor consists of LIG electrodes that are connected by a  $\sim 60\ \mu\text{m}$  wide LIG channel (Figure 2a and b). The Type 2 design thereby does not depend on random filament formation, such as the Type 1 sensor, which accounts for the 100% device yield during fabrication of the Type 2 device. Similar to the working mechanism of the Type 1 device reported in Figure 1, the majority of the power dissipation occurs across the narrow LIG channel. The temperature of the LIG filament during gas sensor operation was estimated to be  $\sim 500\ \text{K}$ , based on the temperature-dependent transport characteristics of LIG (Figure S2), well below the decomposition temperature for LIG in air. Additionally, thermal images were collected for Joule heated LIG and reported in Figure S3a,b, to provide further support that the LIG experiences Joule heating over the relevant power dissipation regime. The ultimate temperature, and sensor sensitivity, of the LIG filament is dependent upon the geometry of the filament. This is because the channel aspect ratio influences the resistance, power dissipation, and hence Joule heating. Additional electrical power can be supplied to increase the sensor sensitivity. An SEM image from the channel region of the Type 2 gas sensor is shown in Figure 2c. The LIG is highly porous and contains a 3D percolating network of nanoscale LIG fibers (Figure 2d). Hence, the high surface area of the LIG fibers enables rapid sensor response to gas molecules.

Figure 3a shows the response of the type 2 sensor with respect to vacuum when exposed to multiple cycles of  $\text{O}_2$  gas, operating at  $\sim 28\ \text{mW}$ . The response is highly repeatable with virtually no variation in the sensitivity. Since the thermal properties of a gas depends upon the gas composition, the extent of convective cooling of the LIG gas sensors should vary with gas composition. Figure 3b shows the sensitivity of the device when exposed to cycles of Air, He, and  $\text{O}_2$ . Importantly, the sensors exhibit response sensitivity to each gas species, and the behavior is repeatable between multiple cycles. However, the vacuum quality in the measurement chamber in between each gas cycle depends on the gas history. For example, inert gas such as Ar will pump more rapidly than air due to the moisture content of the latter. Therefore, the sensor sensitivity for the various gases is reported with respect to the He sensitivity since it is an inert gas with high thermal conductivity. Device sensitivity is highest for He, which has a high relative thermal conductivity ( $\sim 180\ \text{mW m}^{-1}\ \text{K}^{-1}$ ) compared to the other inert gases, while device sensitivity is lower for gases such as Ar that have lower relative thermal conductivity ( $\sim 25\ \text{mW m}^{-1}\ \text{K}^{-1}$ ). This indicates that the

extent of cooling of the LIG filament depends upon the thermal conductivity of the gas species. Thermal conductivity vs temperature for all studied gas species can be found in Figure S6. Due to the high porosity of LIG, the response and recovery characteristics for the sensors are rapid and easily distinguishable.

The repeatability of the Type 2 gas sensors when exposed to many cycles of gas is shown in Figure 3c, and Table S1 provides statistics about device-to-device repeatability. The gas sensor is exposed to  $>50$  cycles of He gas followed by vacuum and experienced standard deviation of 0.16% for each He cycle. This demonstrates that the response of the gas sensor is highly repeatable, thus enabling reliable detection of gas species. Additionally, the gas sensor, which is directly lased into a PI substrate, was subjected to bending to measure flexible sensor reliability. Specifically, the sensor was bent at a radius of curvature of 7 mm for 1000 cycles. Figure 3d reports the sensor sensitivity to air after bending, and the inset shows example sensor responses to air after 0 and 1000 cycles of bending. There are only minor variations in device sensitivity and no discernible degradation of the sensor, thus indicating robust response as a flexible sensor. It is worth noting that LIG can be used as a flexible strain sensor since relatively small displacements can result in a high gauge factor;<sup>14</sup> Therefore, the LIG-based gas sensor will also experience variation in resistivity during the flexing process which would convolute the gas sensing. Hence, the gas sensor should remain static during sensing, or measures should be taken to deconvolute background noise resulting from flexing.

The average sensitivity of 6–10 Type 2 gas sensors to a variety of gases is reported in Figure 4a. The sensitivity of these

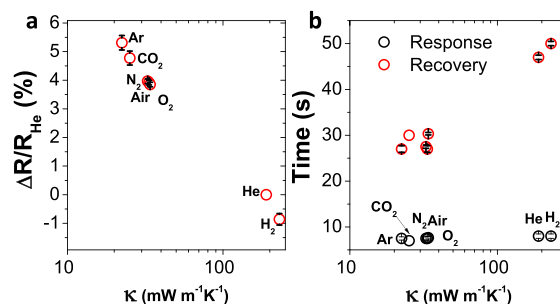
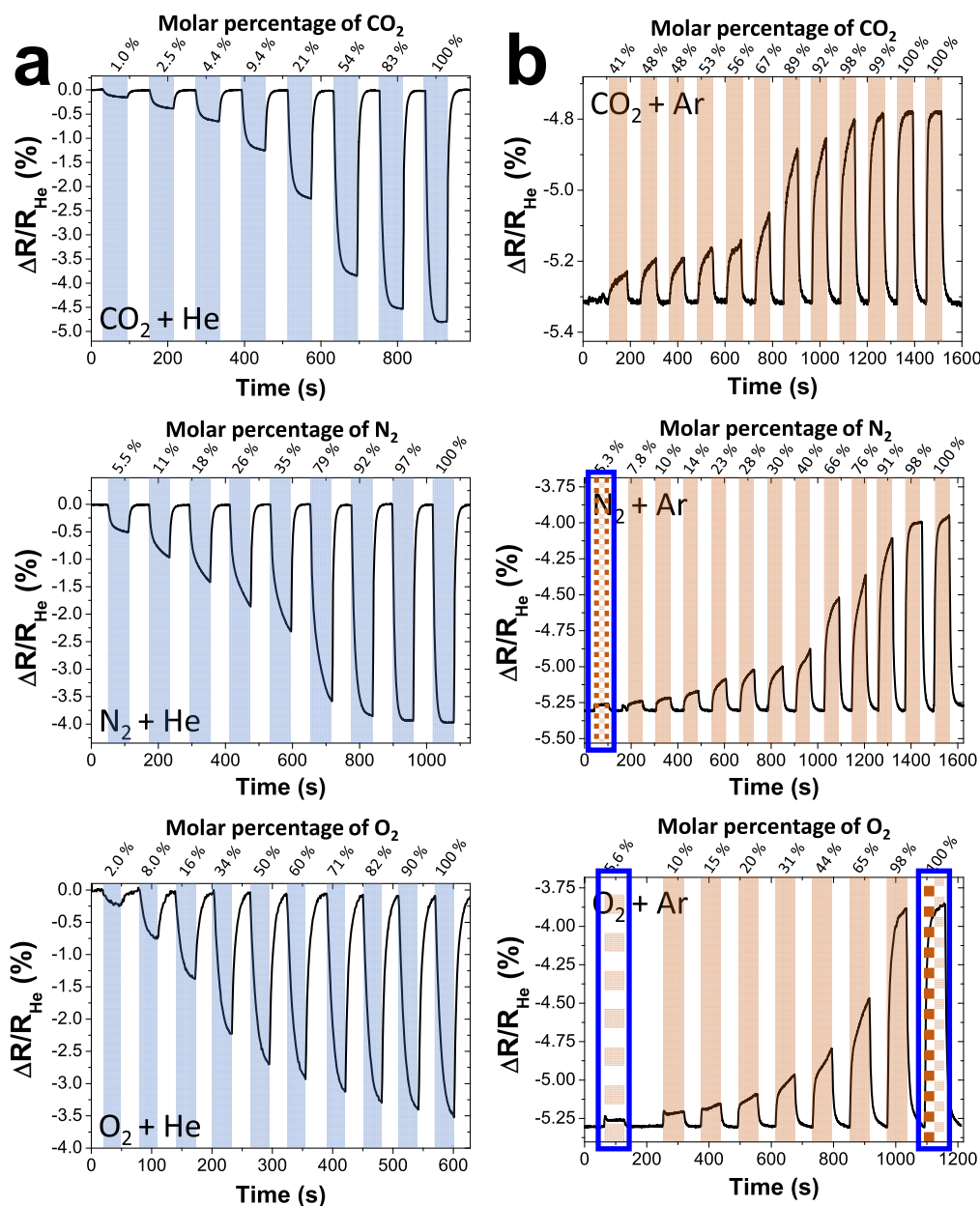


Figure 4. (a) Sensitivity of various gas species normalized to the response of helium gas at maximum operating voltage (12 V). (b) Response and recovery times for devices exposed to various gas species. The black circles are the response times of the sensors when exposed to the various gases. The red circles are the recovery times of the sensors when exposure to the gases is ceased. The response and recovery times are defined as the time required for the sensor to achieve 90% of its sensitivity to a given gas species.

devices is reported with respect to the device sensitivity to He. This was chosen as a reference as opposed to vacuum since the device current under vacuum will largely vary with vacuum quality. Errors bars report the standard error which reflect device to device variability. These values are reported in the Supporting Information (Table S1). Much of the device sensitivity error is attributed to device-to-device variation in the resistance of the LIG sensing channels. Specifically, the average channel resistance and standard deviation was  $389.7 \pm 12.4\ \Omega$ .

The sensor sensitivity scales with the thermal conductivity of the gas species for all gases measured. This enables the sensors



**Figure 5.** (a) Response of the LIG-based gas sensor to varying molar concentrations of CO<sub>2</sub> (top), N<sub>2</sub> (middle), and O<sub>2</sub> (bottom) with He background gas. (b) Response of the LIG-based gas sensor to varying molar concentrations of CO<sub>2</sub> (top), N<sub>2</sub> (middle), and O<sub>2</sub> (bottom) with Ar background gas.

to be used for gas detection for many gas species. Figure 4b reports the response and recovery times for the sensors for each gas species. All response times are on the order of 8 s, and recovery times range from 25 to 50 s. The limiting factor for the response and recovery times is likely the speed at which the gas molecules can be injected and pumped from the test chamber. For example, the gas sensor exhibits a larger recovery time for He and H<sub>2</sub> presumably because of slower pump down speeds in comparison to the other studied gases. The high surface area and high thermal conductivity of LIG makes it an excellent material to achieve fast response times in thermal conductivity sensing applications, and faster response times are expected in comparison to standard TCD technology. In fact, due to the porous nature of LIG, the majority of the material is suspended as opposed to supported by or contacting the substrate. Suspended graphene has demonstrated extremely

high thermal conductivity on the order of  $\sim 5000 \text{ W m}^{-1}\text{K}^{-1}$ .<sup>6</sup> Additionally, the power consumption for these devices ( $\sim 28 \text{ mW}$ ) is low in comparison to other micro-TCDs.<sup>31</sup>

Figure 5 reports the response of a LIG-based gas sensor to varying concentrations of gas mixtures. Specifically, binary gas mixtures of CO<sub>2</sub>, N<sub>2</sub>, and O<sub>2</sub> are demonstrated with He and Ar background gases. Clearly, the sensor can effectively differentiate between subtle gas concentration changes and demonstrates a robust response to a variety of gas mixtures. The gas composition can be quantified by considering the thermal conductivity of a binary gas mixture in eqs 2–4:<sup>32</sup>

$$\kappa_{\text{mix}} = \kappa_1 \left( 1 + G_{12} \frac{x_2}{1 - x_2} \right)^{-1} + \kappa_2 \left( 1 + G_{21} \frac{1 - x_2}{x_2} \right)^{-1} \quad (2)$$

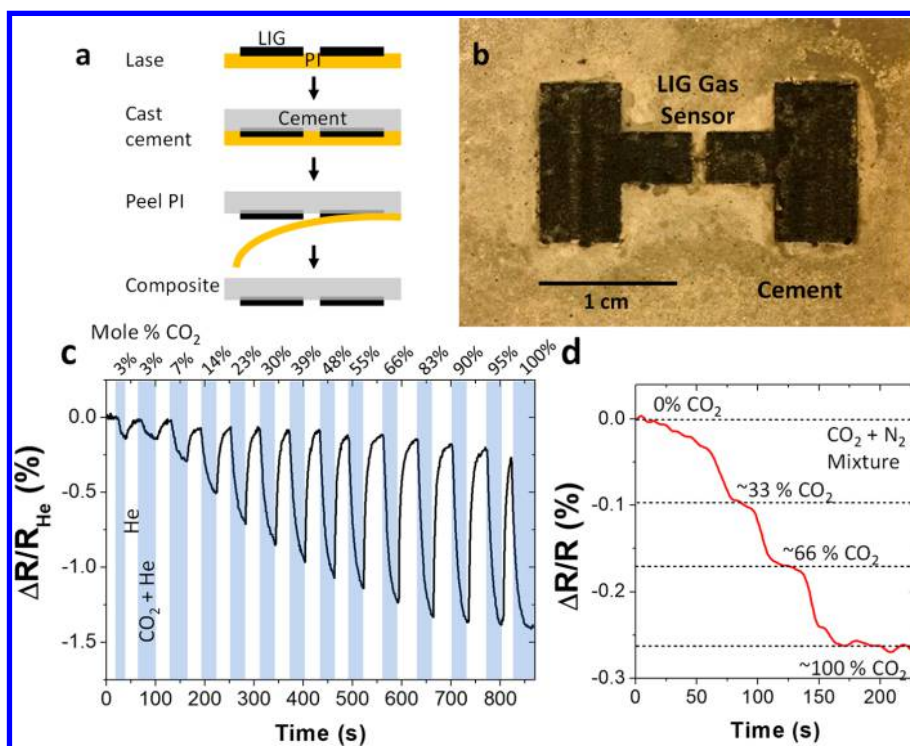


**Figure 6.** (a) Schematic showing the process of embedding a LIG-based sensor into cement. The 50  $\mu\text{m}$  active filament is not drawn for clarity. (b) Optical image of the LIG sensor-embedded in cement. (c) Response of the cement-embedded device to varying molar concentrations of  $\text{CO}_2$  in He ranging from 0% to 100%  $\text{CO}_2$  in He. (d) Response of the cement-embedded device to varying molar concentrations of a  $\text{CO}_2$  and  $\text{N}_2$  gas mixture. These gases are abundant in flue gas.

where,

$$G_{12} = \frac{1.065}{2\sqrt{2}} \left( 1 + \frac{M_1}{M_2} \right)^{-1/2} \left( 1 + \sqrt{\frac{\mu_1}{\mu_2} \left( \frac{M_2}{M_1} \right)^{1/4}} \right)^2 \quad (3)$$

$$G_{21} = \frac{1.065}{2\sqrt{2}} \left( 1 + \frac{M_2}{M_1} \right)^{-1/2} \left( 1 + \sqrt{\frac{\mu_2}{\mu_1} \left( \frac{M_1}{M_2} \right)^{1/4}} \right)^2 \quad (4)$$

$\kappa$  is the thermal conductivity,  $x$  is the molar fraction,  $\mu$  is the viscosity, and  $M$  is molecular weight. As the gas concentration changes, the  $\kappa_{\text{mix}}$  is altered, thus tuning the extent of convective heat transfer ( $q$ ) and hence the response of the gas sensor. The thermal conductivity of the various gas mixtures as a function of concentration is plotted in Figure S7, and Figure S8 reports the sensor response for additional gas mixtures. With the assumption that  $C_p$  is independent of temperature (or experiences modest variation over this temperature range), the change in heat transfer ( $\Delta q$ ) is largely dependent upon  $\kappa_{\text{mix}}$  and hence gas composition. Therefore, the response of the gas sensor is directly correlated to change in gas thermal conductivity, and gas molar composition can be determined in accordance with eq 2. The variation in resistivity of the LIG is approximately linear with temperature, while the response of the gas sensors are not linear with varying concentrations of the gas mixtures. This is because  $\kappa_{\text{mix}}$  as a function of composition is not linear, as reported in eq 2 and Figure S7.

The sensor response for the gas mixtures with He and Ar as background gases demonstrate opposite polarity. This is because He and Ar have drastically different thermal conductivities. Namely, He has relatively high thermal

conductivity, and the LIG filament is cooled effectively. This means that most gas mixtures with He as the background gas will result in an increase in the LIG filament temperature. On the contrary, Ar has a low thermal conductivity. Therefore, most gas mixtures with Ar as the background gas will result in a decrease in the LIG filament temperature. Additional details on the gas concentration calculation can be found in the Supporting Information. The sensor response often did not saturate during the 60 s gas cycle. This is because vacuum conductance in the gas tubing was relatively low and requires several minutes for the gases to achieve an equilibrium mixture concentration. Therefore, the concentration was dynamic during the gas cycle, and the reported concentration represents the maximum analyte concentration during that cycle. Cycling data demonstrating the equilibrium time for the gas mixtures is shown in Figure S9. The detection limits of the gas sensor were also characterized and are reported in Figure S10. The sensor was able to distinguish  $\sim 3600$  ppm Ar in He, and ultimate detection limits are on the order of 100–1000 ppm based on the measurement signal-to-noise.

A flowchart is provided in the Supporting Information (Figure S11) that provides a scheme for how the LIG-based gas sensor can be used to determine composition of a gas mixture or the identity of an unknown gas. Since the gas sensor detects thermal conductivity of a gas or gas mixture, it can be used in sensing applications for virtually any gas; however, there are enormous combinations of gas compositions that can result in a specific thermal conductivity. Therefore, the gas sensor is most useful for determining the identity of a single gas species or determining the composition of a gas mixture in which the identities of the gas species are known.

LIG composites can also be used to generate functional materials. Here LIG was embedded within cement by the method shown in Figure 6a. Specifically, LIG was made by laser on a PI substrate. Portland cement was then cast on top of the PI substrate and allowed to infiltrate the LIG. After curing, the PI substrate was peeled off the Portland cement. Cement intercalation within the large pores in the LIG effectively anchors the LIG into the cement, and the LIG pattern on the PI substrate is thereby transferred to the cement. Conveniently, this enables the formation of embedded electronics without the need to incorporate expensive precious metals. Also, the transfer of LIG into a composite is a simple mechanical process that does not require high energy cost, such as vacuum processing or electroplating. Figure 6b shows the LIG/cement composite-based gas sensor. Embedding LIG devices and circuits directly in a material such as cement can be attractive for a variety of reasons in comparison to adhering a device. For example, the surrounding environment could be corrosive to materials used to attach a sensor or cause degradation of adhesive materials. The refractory nature of the cement is also beneficial for operation of the gas sensor, since the Joule-heated LIG filament will not degrade the mechanical integrity of the material over relevant operating temperatures, and the sensor could withstand high environmental temperatures. SEM images of the embedded LIG sensor are shown in Figure S12.

Figure 6c shows the composition-dependent sensor response when exposed to a gas mixture of He and CO<sub>2</sub>. This demonstrates that the LIG/cement composite gas sensor can be used to determine the composition of a gas mixture. The CO<sub>2</sub> sensitivity (in reference to He) of the Type 2 sensor is reduced from 4.8% to 1.4% in comparison to the devices reported in Figures 3 and 5. This is because the transfer process of the LIG to cement can slightly alter the morphology of the LIG as well as change the thermal mass of the sensor in comparison to PI; however, the sensor can simply be calibrated to the response of gases with varying thermal conductivity, such as in CO<sub>2</sub> vs He.

The incorporation of electronic devices directly into construction materials expands the capabilities of smart composites toward the broader application of the Internet-of-things. For example, gas sensors embedded directly into cement could be applied toward monitoring gases produced by a variety of manufacturing processes. Figure 6d reports the response of the LIG/cement composite gas sensor to varying concentrations of CO<sub>2</sub> and N<sub>2</sub>, which are the two most abundant gases in flue gas. Therefore, gas sensors could be embedded in cement and incorporated in flue gas chimneys to monitor flue gas concentration *in situ*. Embeddable LIG sensors may see other applications in extreme environments. For example, attaching a sensor to a surface via use of a polymeric adhesive may not be compatible with elevated temperatures in which LIG and refractory cement are well-suited. Also, flue gas from coal burning may produce sulfuric acid that is corrosive to common sensor materials such as copper. Embeddable sensors provide a robust alternative.

## CONCLUSION

In summary, flexible LIG-based gas sensors were demonstrated. These gas sensors were fabricated by laser on a PI substrate with a 10.6 μm CO<sub>2</sub> laser. During operation, a potential is applied across the gas sensor that results in heating of a high resistance LIG channel. The gas sensors effectively

measure the thermal conductivity of the surrounding gases. This device structure results in robust sensing capabilities that can be used to sense an array of surrounding gas species, similar to a katharometer. Conveniently, the LIG exhibits a high surface area of ~350 m<sup>2</sup> g<sup>-1</sup>, and high thermal conductivity characteristic of graphene. Therefore, rapid response times of 7–8 s were recorded for all test gas species, and the response times were likely limited by the injection rate of gas molecules into the test chamber. Due to the high porosity of LIG, gas sensors could easily be transferred to other matrices by a transfer process described here. A LIG/cement composite gas sensor was demonstrated which could be used to determine compositions of a gas mixture. For data analysis, it would be most simple to operate in relatively static conditions. For example, the gas temperature will influence thermal conductivity and hence the sensor response. However, temperature dependence on the thermal conductivity of most gas species are well documented and this can be factored into the sensor response. Additionally, water vapor will influence the thermal conductivity of a gas mixture. The thermal conductivity of water vapor is well documented, so this can be added to the analysis. Water vapor should not condense on the LIG filament during operation since it would be operating well above the water vaporization temperature. Any gas species that can provide a detectable change in the thermal conductivity of a gas mixture can be sensed using the gas sensor. However, the LIG filaments should be guarded from solid particles that could become embedded within the LIG and affect the thermal mass. This could alter the sensitivity of the sensor. This advance will enable the incorporation of carbon-based electronics in a variety of substrates and expand the capabilities of smart materials, including for the real-time monitoring of CO<sub>2</sub> and gas ratios in flue gas.

## METHODS

**Synthesis of LIG.** LIG was synthesized by laser on commercially available PI (McMaster-Carr, Kapton Polyimide Film, 0.005" thick) with a Universal Laser Systems XLS10MWH laser platform. The laser system is equipped with a 75 W pulsed CO<sub>2</sub> laser (10.6 μm). A scanning speed of 18 cm s<sup>-1</sup> was used with a duty cycle of 1%. An image density of 1000 pulses per inch (PPI, a standard setting on commercial systems; 1 in. = 2.54 cm) was applied for all sensors. These laser conditions result in superhydrophilic LIG.

**Fabrication of Devices.** Devices were fabricated with LIG serving as the electrode materials as well as the gas sensing filament. Two different device structures are reported in this manuscript. The first structure (Type 1) relies on patterning LIG electrodes with a < 50 μm PI gap between electrodes. Small LIG flakes generated from the laser process span the gap between electrodes. The second device structure (Type 2) demonstrates increased reliability by incorporating an intentionally patterned continuous LIG filament. The sensing filament is patterned with a width of 50 μm and a length of 300 μm. Due to the need for LIG flakes to span a gap between electrodes, the yield for fabricating functioning Type 1 devices was ~20% (2 of 10), whereas the yield for functioning Type 2 devices was 100% across 10 sensors that were made and tested. LIG electrode regions were coated with silver paint and copper tape to ensure adequate electrical contacts.

**Characterization of Devices.** Devices were characterized in a Desert Cryogenics model CPX-VF vacuum probe station. This probe station is outfitted with a stage heater as well as roughing and turbomolecular vacuum pumps. Gas sensing measurements were recorded after pumping the chamber under vacuum for approximately 30 min. The following gases were plumbed into the probe station to back-flow into the chamber: H<sub>2</sub>, He, Air, O<sub>2</sub>, N<sub>2</sub>, Ar, and CO<sub>2</sub>. The chamber was open to the roughing pump during gas introduction to

ensure gas flow at room temperature. Thereafter the chamber pressure was held at approximately 200 mbar during sensor characterization. Device responses were recorded by applying a constant voltage across the device and measuring the current when exposed to a variety of gas species. Change in resistance of the device was determined from the changes in device current. Electrical characterization was conducted using an Agilent Semiconductor Parameter Analyzer model B1500A.

**LIG/Portland Cement Composite.** LIG/Portland cement composite was fabricated by first lasing PI with the 10.6  $\mu\text{m}$  laser to synthesize LIG. The PI film was then placed in a mold that was subsequently filled with Portland cement. The composite was allowed to cure for  $\sim 48$  h at 90  $^{\circ}\text{C}$  in the presence of water to ensure hydration of the cement. The PI film was peeled off of the cured composite, thus leaving the LIG embedded in the Portland cement.

## ASSOCIATED CONTENT

### Supporting Information

The Supporting Information is available free of charge on the ACS Publications website at DOI: [10.1021/acsnano.8b09622](https://doi.org/10.1021/acsnano.8b09622).

TGA, temperature-dependent electrical transport, images of Joule heated LIG, additional gas sensor sensitivity plots, SEM images, gas thermal conductivity calculations, and gas sensor detection sensitivity (PDF)

## AUTHOR INFORMATION

### Corresponding Author

\*E-mail: [tour@rice.edu](mailto:tour@rice.edu).

### ORCID

James M. Tour: [0000-0002-8479-9328](https://orcid.org/0000-0002-8479-9328)

### Notes

The authors declare the following competing financial interest(s): Rice University owns intellectual property (IP) on the LIG process. The IP is being licensed to a company in which none of the authors are officers or directors, but J.M.T. will be a stockholder. All potential conflicts are disclosed to and managed by the Rice University Office of Sponsored Projects and Research Compliance.

## ACKNOWLEDGMENTS

The Air Force Office of Scientific Research (FA9550-14-1-0111) provided funding. We gratefully acknowledge the support of Universal Laser Systems for their generously providing the XLS10MWH laser system with Multiwave Hybrid technology that was used for this research. The Universal Laser Systems staff kindly provided helpful advice. John Li is acknowledged for assisting with data acquisition.

## REFERENCES

- (1) Geim, A. K.; Novoselov, K. S. The Rise of Graphene. *Nat. Mater.* **2007**, *6*, 183–191.
- (2) Geim, A. K. Graphene: Status and Prospects. *Science* **2009**, *324*, 1530–1534.
- (3) Bolotin, K. I.; Sikes, K. J.; Jiang, Z.; Klima, M.; Fudenberg, G.; Hone, J.; Kim, P.; Stormer, H. L. Ultrahigh Electron Mobility in Suspended Graphene. *Solid State Commun.* **2008**, *146*, 351–355.
- (4) Yan, Z.; Peng, Z.; Casillas, G.; Lin, J.; Xiang, C.; Zhou, H.; Yang, Y.; Ruan, G.; Raji, A.-R. O.; Samuel, E. L. G.; et al. Rebar Graphene. *ACS Nano* **2014**, *8*, 5061–5068.
- (5) Li, Y.; Peng, Z.; Larios, E.; Wang, G.; Lin, J.; Yan, Z.; Ruiz-Zepeda, F.; José-Yacamán, M.; Tour, J. M. Rebar Graphene from Functionalized Boron Nitride Nanotubes. *ACS Nano* **2015**, *9*, 532–538.
- (6) Ghosh, S.; Calizo, I.; Teweldebrhan, D.; Pokatilov, E. P.; Nika, D. L.; Balandin, A. A.; Bao, W.; Miao, F.; Lau, C. N. Extremely High

Thermal Conductivity of Graphene: Prospects for Thermal Management Applications in Nanoelectronic Circuits. *Appl. Phys. Lett.* **2008**, *92*, 151911.

(7) Lin, J.; Peng, Z.; Liu, Y.; Ruiz-Zepeda, F.; Ye, R.; Samuel, E. L. G.; Yacamán, M. J.; Yakobson, B. I.; Tour, J. M. Laser-Induced Porous Graphene Films from Commercial Polymers. *Nat. Commun.* **2014**, *5*, 5714.

(8) Li, Y.; Luong, D. X.; Zhang, J.; Tarkunde, Y. R.; Kittrell, C.; Sargunraj, F.; Ji, Y.; Arnusch, C. J.; Tour, J. M. Laser-Induced Graphene in Controlled Atmospheres: From Superhydrophilic to Superhydrophobic Surfaces. *Adv. Mater.* **2017**, *29*, 1700496.

(9) Duy, L. X.; Peng, Z.; Li, Y.; Zhang, J.; Ji, Y.; Tour, J. M. Laser-Induced Graphene Fibers. *Carbon* **2018**, *126*, 472–479.

(10) Ye, R.; Han, X.; Kosynkin, D. V.; Li, Y.; Zhang, C.; Jiang, B.; Marti, A. A.; Tour, J. M. Laser-Induced Conversion of Teflon into Fluorinated Nanodiamonds or Fluorinated Graphene. *ACS Nano* **2018**, *12*, 1083–1088.

(11) Peng, Z.; Lin, J.; Ye, R.; Samuel, E. L. G.; Tour, J. M. Flexible and Stackable Laser-Induced Graphene Supercapacitors. *ACS Appl. Mater. Interfaces* **2015**, *7*, 3414–3419.

(12) Zang, X.; Shen, C.; Chu, Y.; Li, B.; Wei, M.; Zhong, J.; Sanghadasa, M.; Lin, L. Laser-Induced Molybdenum Carbide-Graphene Composites for 3D Foldable Paper Electronics. *Adv. Mater.* **2018**, *30*, 1800062.

(13) Zhang, Z.; Song, M.; Hao, J.; Wu, K.; Li, C.; Hu, C. Visible Light Laser-Induced Graphene from Phenolic Resin: A New Approach for Directly Writing Graphene-Based Electrochemical Devices on Various Substrates. *Carbon* **2018**, *127*, 287–296.

(14) Luo, S.; Hoang, P. T.; Liu, T. Direct Laser Writing for Creating Porous Graphitic Structures and Their Use for Flexible and Highly Sensitive Sensor and Sensor Arrays. *Carbon* **2016**, *96*, 522–531.

(15) Sun, B.; McCay, R. N.; Goswami, S.; Xu, Y.; Zhang, C.; Ling, Y.; Lin, J.; Yan, Z. Gas-Permeable, Multifunctional On-Skin Electronics Based on Laser-Induced Porous Graphene and Sugar-Templated Elastomer Sponges. *Adv. Mater.* **2018**, *30*, 1804327.

(16) Zhang, J.; Ren, M.; Li, Y.; Tour, J. M. *In Situ* Synthesis of Efficient Water Oxidation Catalysts in Laser-Induced Graphene. *ACS Energy Lett.* **2018**, *3*, 677–683.

(17) Zhang, J.; Zhang, C.; Sha, J.; Fei, H.; Li, Y.; Tour, J. M. Efficient Water-Splitting Electrodes Based on Laser-Induced Graphene. *ACS Appl. Mater. Interfaces* **2017**, *9*, 26840–26847.

(18) Zhang, J.; Ren, M.; Wang, L.; Li, Y.; Yakobson, B. I.; Tour, J. M. Oxidized Laser-Induced Graphene for Efficient Oxygen Electrocatalysis. *Adv. Mater.* **2018**, *30*, 1707319.

(19) Ye, R.; James, D. K.; Tour, J. M. Laser-Induced Graphene: From Discovery to Translation. *Adv. Mater.* **2019**, *31*, 1803621.

(20) Ye, R.; James, D. K.; Tour, J. M. Laser-Induced Graphene. *Acc. Chem. Res.* **2018**, *51*, 1609–1620.

(21) Wang, T.; Huang, D.; Yang, Z.; Xu, S.; He, G.; Li, X.; Hu, N.; Yin, G.; He, D.; Zhang, L. A Review on Graphene-Based Gas/Vapor Sensors with Unique Properties and Potential Applications. *Nano-Micro Lett.* **2016**, *8*, 95–119.

(22) Singh, E.; Meyyappan, M.; Nalwa, H. S. Flexible Graphene-Based Wearable Gas and Chemical Sensors. *ACS Appl. Mater. Interfaces* **2017**, *9*, 34544–34586.

(23) Mackin, C.; Schroeder, V.; Zurutuza, A.; Su, C.; Kong, J.; Swager, T. M.; Palacios, T. Chemiresistive Graphene Sensors for Ammonia Detection. *ACS Appl. Mater. Interfaces* **2018**, *10*, 16169–16176.

(24) Shokuhi Rad, A.; Esfahanian, M.; Maleki, S.; Gharati, G. Application of Carbon Nanostructures toward  $\text{SO}_2$  and  $\text{SO}_3$  Adsorption: A Comparison between Pristine Graphene and N-Doped Graphene by DFT Calculations. *J. Sulfur Chem.* **2016**, *37*, 176–188.

(25) Al-Mashat, L.; Shin, K.; Kalantar-zadeh, K.; Plessis, J. D.; Han, S. H.; Kojima, R. W.; Kaner, R. B.; Li, D.; Gou, X.; Ippolito, S. J.; et al. Graphene/Polyaniline Nanocomposite for Hydrogen Sensing. *J. Phys. Chem. C* **2010**, *114*, 16168–16173.

- (26) Pearce, R.; Iakimov, T.; Andersson, M.; Hultman, L.; Spetz, A. L.; Yakimova, R. Epitaxially Grown Graphene Based Gas Sensors for Ultra Sensitive NO<sub>2</sub> Detection. *Sens. Actuators, B* **2011**, *155*, 451–455.
- (27) Karasek, F. W.; Clement, R. E. *Basic Gas Chromatography-Mass Spectrometry: Principles and Techniques*; Elsevier: Amsterdam, The Netherlands, 2012.
- (28) Daynes, H. A.; Shakespear, G. A. The Theory of the Katharometer. *Proc. R. Soc. London, Ser. A* **1920**, *97*, 273–286.
- (29) Ferrari, A. C.; Meyer, J. C.; Scardaci, V.; Casiraghi, C.; Lazzeri, M.; Mauri, F.; Piscanec, S.; Jiang, D.; Novoselov, K. S.; Roth, S.; Geim, A. K. Raman Spectrum of Graphene and Graphene Layers. *Phys. Rev. Lett.* **2006**, *97*, 187401.
- (30) Bird, R. B. Transport Phenomena. *Appl. Mech. Rev.* **2002**, *55*, R1.
- (31) Narayanan, S.; Alfeeli, B.; Agah, M. A Micro Gas Chromatography Chip with an Embedded Non-Cascaded Thermal Conductivity Detector. *Procedia Eng.* **2010**, *5*, 29–32.
- (32) Mason, E. A.; Saxena, S. C. Approximate Formula for the Thermal Conductivity of Gas Mixtures. *Phys. Fluids* **1958**, *1*, 361–369.